A Competition of Secondary and Primary Nucleation Controls Amyloid Fibril Formation of the Parathyroid Hormone

*Bruno Voigt, Maria Ott, and Jochen Balbach**

Functional amyloids belong to an increasing class of non-toxic biologic material, in contrast to the prominent disease-related amyloids. Herein, this work reports on the fibril formation of the parathyroid hormone PTH_{84} as a representative candidate following the same generic principles of primary and secondary nucleation. Employing Thioflavin T monitored kinetics analyses and negative-staining transmission electron microscopy, an intricate, concentration dependent behavior of time dependent generation and morphologies of PTH_{84} fibrils are found. While at low peptide concentrations, fibril formation is driven by surface catalyzed secondary nucleation, an increased amount of peptides cause a negative feedback on fibril elongation and secondary nucleation. Moreover, the source of primary nuclei is found to regulate the overall macroscopic fibrillation. As a consequence, the concentration dependent competition of primary versus secondary nucleation pathways is found to dominate the mechanism of fibril generation. This work is able to hypothesize an underlying monomer-oligomer equilibrium providing high-order species for primary nucleation and, additionally, negatively affecting the available monomer pool.

1. Introduction

Amyloid fibrils play key roles in disease and physiological function.[1,2] An increasing number of so-called functional amyloids had been identified, for which the fibrillar state is not a pathological form of the corresponding protein but has its own

B. Voigt, J. Balbach
Institute of Physics
Martin Luther University Halle-Wittenberg
Betty-Heimann-Strasse 7, DE-06120 Halle, Germany
E-mail: jochen.balbach@physik.uni-halle.de
M. Ott
Institute of Biochemistry and Biotechnology
Martin Luther University Halle-Wittenberg
Kurt-Mothes-Strasse 3, DE-06120 Halle, Germany

biological function. An important feature is the, at least partial, reversibility of fibril formation and thus a controlled monomer release. Among others, functional amyloids have implications in bacterial biofilm, human skin pigmentation, memory and peptide hormone storage.[3–6] For the latter task, peptide hormones are synthesized as monomers, and subsequently stored in secretory granules. Upon release into the blood stream, monomers dissociate from fibril ends and can thus act on their targets.[7–9] For β-endorphin it has been shown for example that a pH jump (from acidic granule into alkaline blood) in combination with a drop in peptide concentration due to dilution triggers the monomer release.[10]

Tracking the kinetics of amyloid formation, for example, by the small organic dye Thioflavin T (ThT) monitoring the fibrillar mass, results in a sigmoidal shape build up curve when starting from peptide monomers. The time evolution comprises a lag-phase, a growth phase and a stationary phase at which the system approaches an equilibrium state.[11,12] Intensive work over the last decades revealed that this simple macroscopic behavior originates from an intricate network of different individual molecular mechanisms.[13] These are typically classified into processes increasing the fibrillar mass M (elongation) and the number of fibrils P (**Figure 1**). The latter comprises primary (primary nucleation) and secondary events (secondary nucleation, fragmentation). The contribution of these individual microscopic pathways for a certain system and the respective rate constants defines the macroscopic curve shape as well as its dependence on the peptide concentration.[14,15]

The parathyroid hormone is a peptide hormone acting in Ca^{2+} and phosphate homeostasis which gets produced by the parathyroid glands as a pre-pro-hormone of 115 amino acids.[18,19] The 25 residue pre sequence is cleaved co-translationally, while the six residue pro-sequence is cleaved by the endopeptidase furin in the Golgi apparatus.[20,21] The mature hormone, being referred to as PTH_{84}, comprises of 84 amino acids. The N-terminal 34 amino acids exhibit an α-helical propensity whereas the C-terminus remains intrinsically disordered.[22,23] In previous in vitro studies we demonstrated that PTH_{84} undergoes spontaneous fibrillar self-assembly at neutral and alkaline conditions
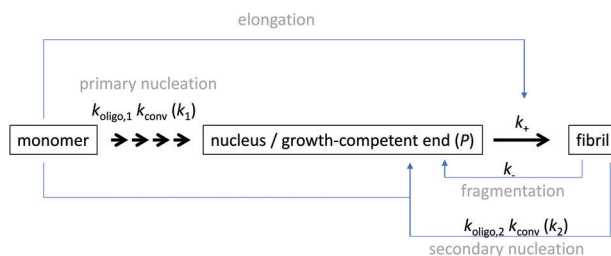
Figure 1. Simplified microscopic processes involved in macroscopic amyloid fibril formation.[16] New fibrils (one fibril/seed is assumed to have two growth-competent ends, P) are generated by primary (primary nucleation – k_1) or secondary processes (secondary nucleation – k_2, fragmentation – k_-). The increase of fibrillar mass M occurs mainly via elongation of growth-competent ends, k_+, by the addition of, in most cases, monomers. The mass increase due to nucleation is typically neglected in the analysis. In this work, we use a three-step kinetic model treating k_1 as $k_{oligo,1} k_{conv}$ and k_2 as $k_{oligo,2} k_{conv}$ (see Experimental section).[17]

(pH7.4 and pH9.0).[22,24] Under physiological context, on the other hand, no spontaneous fibril formation is observed.[25] Instead, glycose-amino-glycans (GAG), such as heparin, can act as a trigger molecule initializing amyloid fibril formation. The role of GAGs in assisting fibril formation is also known for other amyloidogenic peptides.[6,26] Moreover, PTH$_{84}$ fibrils are the hypothesized storage form of the hormone in analogy to various peptide hormones from the pituitary gland.[6,22,27]

This work was performed as part of project A12 of the Collaborative Research Center Transregio CRC-TRR 102 "Polymers under multiple constraints." There, we focused on the polymer and biophysical properties of PTH$_{84}$ and polymer hybrid-molecules. The latter included covalent conjugates of synthetic polymers with PTH$_{84}$ or the Alzheimer peptide Aβ_{1-40}. PTH$_{84}$ conjugates showed a shroud-like polymer conformation and the polymer stimulated the nucleation process of the peptide hormone.[24] A systematic variation of the physicochemical properties of the synthetic polymer allowed to elucidate how the molecular mass and hydrophilicity/hydrophobicity influenced the kinetics and morphology of amyloid fibrils of Aβ_{1-40}.[28,29]

Further, we have engineered β-turn mimetic conjugates containing synthetic turn mimetic structures in the turn region of Aβ_{40} and Aβ_{16-35}, replacing two amino acids in the turn-region G25 – K28.[30] The structure of the turn mimic induces both, acceleration of fibrillation and the complete inhibition of fibrillation, confirming the importance of the turn region on the aggregation using either a bicyclic β-turn mimetic (BTD) or an artificial aromatic β-turn (TAA), while positions N27-K28 and V24-G25 showed only weaker or no inhibitory effects. A catalytic effect on the fibrillation or inhibition of native Aβ_{40} was observed even when added in amounts down to a 1/10 ratio.

Using a reversibly photo-switchable group we could control the bioavailability of the fibrillating parathyroid hormone (PTH$_{1-84}$)-derived peptide.[31] We have embedded the azobenzene derivate 3-{[(4-aminomethyl)phenyl]diazenyl}benzoic acid (3,4′-AMPB) into the PTH-derived peptide PTH$_{25-37}$ to generate the artificial peptide AzoPTH$_{25-37}$, which can be reversibly photo-switched between its *cis* and *trans* forms. The *trans*-form of AzoPTH$_{25-37}$ is fibrillating similar to PTH$_{25-37}$, while the *cis*-form of AzoPTH$_{25-37}$ generates only amorphous aggregates. Fur-

thermore *cis*-AzoPTH$_{25-37}$ catalytically inhibits the fibrillation of PTH$_{25-37}$ in ratios down to 1/5, opening an approach to catalytically control fibrillation in vivo by an added photo-switchable peptide.[31]

In the present work we report on a biophysical study aiming to investigate the spontaneous self-assembly of PTH$_{84}$ at neutral pH. Under these conditions, a long lag-phase ensured the concentration dependent investigations of fibril elongation and secondary processes since primary nucleation plays a minor role in this time regime.

2. Results and Discussion

2.1. PTH$_{84}$ Undergoes Spontaneous Amyloid Fibril Formation Only at Elevated Peptide Concentrations

One main key to elucidate the different mechanisms of fibril formation is the investigation of peptide concentration dependent fibril formation kinetics. For this purpose, we conducted aggregation experiments starting from freshly purified, monomeric PTH$_{84}$ at initial monomer concentrations c_0 ranging from 50 to 600 μM. The need of high peptide concentrations to obtain fibrils was already shown in previous studies and is closely linked to the reported critical concentration of $c_c = 74 \pm 25$ μM for PTH$_{84}$.[22,24] We obtained curves characteristic for amyloid fibril formation with a lag phase, a sigmoidal growth phase and a plateau phase at which the system approaches its thermodynamic equilibrium (**Figure 2**A). Interestingly and despite the high concentrations used, we found the lag times (time without significant fluorescence increase) with $t_{lag} > 50$ h to be very long compared to, for example, Aβ_{40} ($t_{lag} < 10$ h for $c_0 < 10$ μM, depending on the exact conditions) followed by a relatively long growth phase.[32] In addition, a notable feature of the fibrillation profiles is a double-sigmoidal character at low c_0 (<200 μM, Figure 2A and Figure S1A, Supporting Information). We suspect that, at least, two distinguishable kinetic components with distinct rate constants contribute to the overall fibrillation curves.

However, for samples with c_0 above 200 μM the sigmoidal growth is followed by a decrease of the ThT fluorescence signal before finally reaching a plateau. Interestingly, the final fluorescence values are constant ($F_{ThT} = 8411 \pm 1904$ a. u.), while the maximum signal revealed two linear regimes, with an intercept at 383 μM (Figure 2B). We suspect that these segments hint toward distinct fibril morphologies displaying unique ThT binding behavior. The mean of the final fluorescence overlaps with the maximum fluorescence at $c_0 = 230$ μM. Moreover, the fluorescence decrease can be described by a mono-exponential decay with a rate constant k_{dec} of 0.01 ± 0.005 h^{-1} (Equation (6)) without any dependence on c_0 (Figure 2D, inset). Hence, the decay results from a fibril dependent, rather than a monomer dependent, process, such as the assembly of fibrils into clusters. Images taken from the plate after 310 h incubation indeed proof the existence of precipitates large enough to lead to a turbid sample (Figure S1D, Supporting Information). Static light scattering experiments supported the presence of large particles by displaying an increase of the optical density at 600 nm (OD_{600}, Figure S1E,F, Supporting Information). Interestingly, we observed a shift of the maximum ThT absorbance toward higher wavelengths at high c_0 (Figure S1G, Supporting Information), indicating a change within the
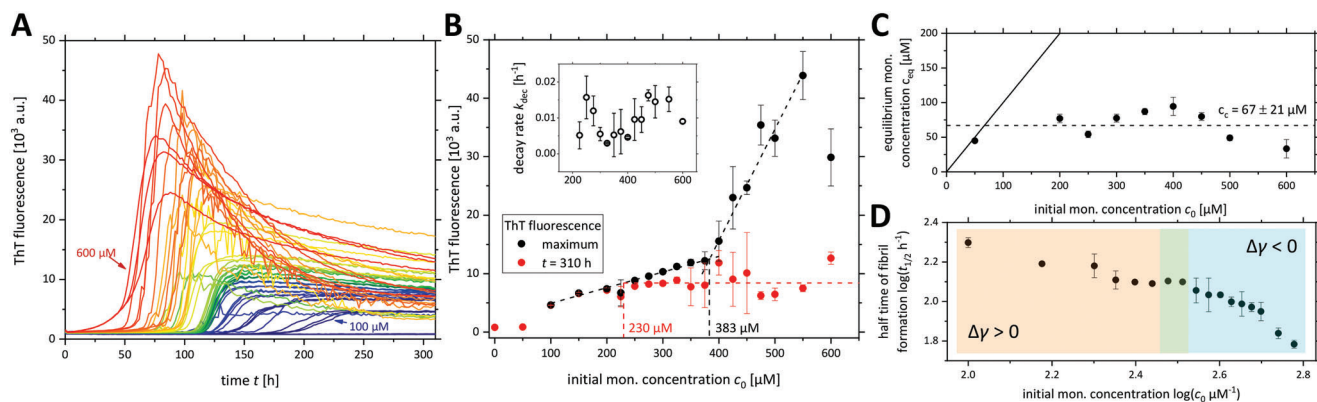
**ADVANCED
SCIENCE NEWS**

www.advancedsciencenews.com

[M] acro-
olecular

Bioscience

www.mbs-journal.de

Figure 2. Amyloid fibril formation by PTH_{84}. A) ThT monitored fibrillation kinetics for the concentration range between 0 and 600 µM in steps of 25 or 50 µM. For 0 and 50 µM no ThT fluorescence increase was detected. All triplicates for each c_0 are shown. B) Average ThT fluorescence at the curve maximum (black) and at $t = 310$ h (red) with respect to c_0. Black dashed lines mark the two linear regimes of the maximum fluorescence. The red dashed line indicates the average end-point fluorescence for $c_0 > 200$ µM. Inset: mono-exponential rate constant k_{dec} of the fluorescence decay after passing the maximum (Equation (6)). C) Equilibrium free monomer concentrations c_{eq} after 310 h. The critical concentration c_c (dashed line) was calculated as the mean of all c_{eq} (for $c_0 > 74$ µM).[22] The solid line indicates the case of no fibril formation ($\bar{c}_{eq} = c_0$). D) log($t_{1/2}$)-log(c_0)-plot of the half time of fibril formation ($t_{1/2}$). The shaded regions indicate positive (orange) and negative (cyan) curvature. All data points in B)–D) represent the mean and the standard deviation of three individual replicates.

molecular environment of the dye or a different binding behavior of ThT leading to distinct fluorescence quantum yields. We determined the concentration of free ThT after fibrillation (after centrifugation of the fibrils) which we found to be inversely proportional to c_0 (Figure S1H, Supporting Information), indicating that bound ThT sedimented together with the fibrils. Conversely, the ThT concentration in the control sample yielded only 35 µM. However, we checked the concentration at the beginning of the experiment (indicated by black dotted line). The decrease of detectable dye molecules could be due to micelle formation of ThT which precipitated during centrifugation.[33] Another possibility would be self-quenching of ThT fluorescence due to an increase of the local dye concentrations leading to the observed fluorescence decrease (Figure 2B).[34,35]

The critical concentration of amyloid formation, c_c, is a parameter reflecting the thermodynamic stability of amyloid fibrils.[36] Therefore, we additionally measured the concentration of free PTH_{84} monomers in equilibrium with fibrils after 310 h. The equilibrium free monomer concentration c_{eq} was consistently found to be 67 ± 21 µM, reflecting the critical concentration c_c (Figure 2C). This agrees with our previous studies as well as with the general concept of the critical concentration and monomer release from functional hormone fibrils.[22,36]

An analysis of the times to half completion of fibrillation profiles (half times, $t_{1/2}$) is a powerful tool to obtain initial information on the dominating mechanisms as well as on corresponding reaction orders.[16] The scaling exponent γ of a log($t_{1/2}$)-log(c_0)-plot can be extracted as a power law with $t_{1/2} \approx c_0^\gamma$. In general, a single consistently dominant mechanism is characterized by a linear scaling, while a competition between two processes typically results in a negative curvature ($\Delta\gamma < 0$). On the other hand, a positive curvature ($\Delta\gamma > 0$) indicates saturation effects, presumably of elongation or secondary nucleation. Here we analyzed the fibrillation kinetics until the maximum ThT fluorescence emission had reached. Interestingly, for PTH_{84} at various initial monomer concentrations we found a positive as well as

a negative curvature of the corresponding half time plot (Figure 2D). This complex behavior has yet only been reported for the $Tau_{304-380}$ fragment but it has not been further elucidated.[37] The positive curvature dominates at $c_0 < 300$ µM, with a scaling exponent increasing from $\gamma \approx -0.5$ to $\gamma = 0$ (indicated by shaded orange region). This agrees with a saturation of the elongation process. The observed negative curvature at $c_0 > 300$ µM (shaded cyan region) denotes the entrance of a process generating additional growth-competent ends into the reaction network. In principle, primary and secondary nucleation need to be considered.

2.2. PTH_{84} Fibrils Display a Strong Polymorphism

We further aimed to investigate the morphology of the fibrils at low (100 µM, **Figure 3**A), intermediate (300 µM, Figure 3B) and high c_0 (500 µM, Figure 3C) by negative staining transmission electron microscopy. The micrographs show curvilinear fibrils characteristic for PTH_{84} as previously reported.[22,24,25] The fibrils are up to several µm in length, only showing few shorter individual fibrils. Notably, PTH_{84} fibrils exhibit a strong polymorphism. Fibrils can be found to be twisted or flat, with an irregular pitch length even in strongly twisted fibrils. Additionally, at 500 µM we found the fibrils to be clustered with only few individual fibrils (Figure 3C, upper panel). In a sample isolated 20 h after the fluorescence maximum was reached in the kinetic assay (Figure S1B, Supporting Information) as well as in a sample treated with probe-sonication (Figure S1C, Supporting Information) an essentially lower amount of these clusters is observed. Both samples exhibit the same macroscopic appearance as for 300 µM at the end-point (compare to Figure 3B). Taken together with the observed fluorescence decrease (Figure 2B), this supports the hypothesis of the formation of supramolecular fibril clusters with impaired ThT fluorescence. Thus, unclustered fibrils essentially contribute to the final ThT fluorescence signal. Since fibril
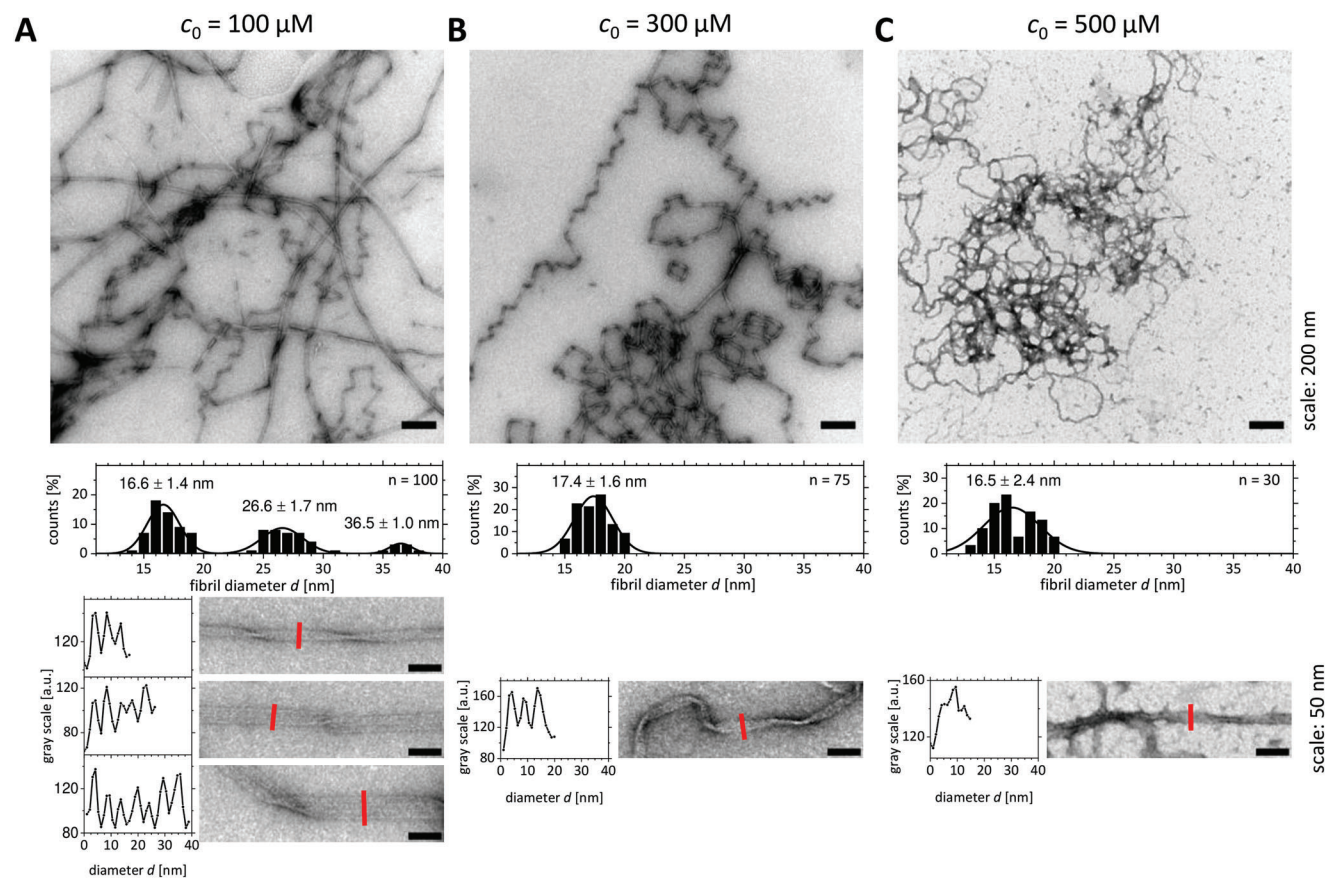
2200525 (3 of 11)

Figure 3. Electron Microscopy reveals polymorphism of PTH_{84} fibrils. Fibril morphologies after 310 h incubation time have been characterized for A) c_0 = 100 μM, B) c_0 = 300 μM and C) c_0 = 500 μM. Shown are representative electron micrographs (upper panel, scale bar = 200 nm), calculation of fibril diameters (middle panel) as well as fibril cross sections (lower panel, left – gray scale, right – representative individual fibril, scale bar = 50 nm, red solid lines indicate cross sections).

precipitation occurs above a threshold concentration of c_0 = 230 μM (Figure 2B), we propose a maximum soluble fibril fraction of 230−67 μM = 163 μM (given in monomer equivalents converted into fibrils, with c_c = 67 μM as the fraction of soluble monomers) in equilibrium with free monomers.

A more detailed analysis of the fibril dimension revealed a consistent diameter of d_{300} = 17.4 ± 1.6 nm for 300 μM and of d_{500} = 16.5 ± 2.4 nm for 500 μM, whereas three different species with $d_{100,1}$ = 16.6 ± 1.4 nm, $d_{100,2}$ = 26.6 ± 1.7 nm and $d_{100,3}$ = 36.5 ± 1.0 nm were found for 100 μM (Figure 3A–C, middle panels). An inspection of the cross sections shows that the fibrils consist of three ($d_{100,1}$, d_{300}, d_{500}), five ($d_{100,2}$), or seven ($d_{100,3}$) individual filamentous structures of about 5.5 nm width within a fibril (Figure 3A–C, bottom panels). The occurrence of three fibrillar sub-types gives rise to the assumption of different underlying kinetic rate constants of fibril formation, as observed for low c_0 (Figure S1A, Supporting Information). However, in a previous study using heparin as fibrillation trigger no polymorphism was observed.[25] Heparin possibly favors the formation of only one morph which we also found for all probed c_0. The morphology of fibrils present in vivo within the secretory granules is currently unknown but their characterization is part of our future work.

2.3. PTH_{84} Fibril Formation is Dominated by Secondary Processes and Inhibition Effects

2.3.1. Light Seeding Demonstrates the Importance of Autocatalytic Self-replication

We further investigated whether secondary processes contribute to the macroscopic fibrillation behavior. Therefore, we repeated the experiment presented in Figure 2A with the addition of a low amount of pre-formed probe-sonicated seeds (0.2 % of c_0, given in monomer equivalents) at time zero (**Figure 4**A, curves for all c_0 are shown in Figure S2A, Supporting Information). For seeded experiments, c_0 denotes the initial concentration of monomeric peptide to which pre-formed seeds are added. If secondary events (secondary nucleation or fragmentation) do not contribute to the overall time course no significant acceleration of fibrillation is expected for a given c_0 compared to the corresponding de novo experiment. Instead, we found a strong reduction of the lag times for all c_0, underlying the importance of secondary events, and thus the autocatalytic self-propagation, for the fibrillation of PTH_{84}. Moreover, we found a linear scaling in the half-time plot with $\gamma = -0.75$, indicating that the saturation and competition effects, as observed for de novo fibrillation (Figure 2D),
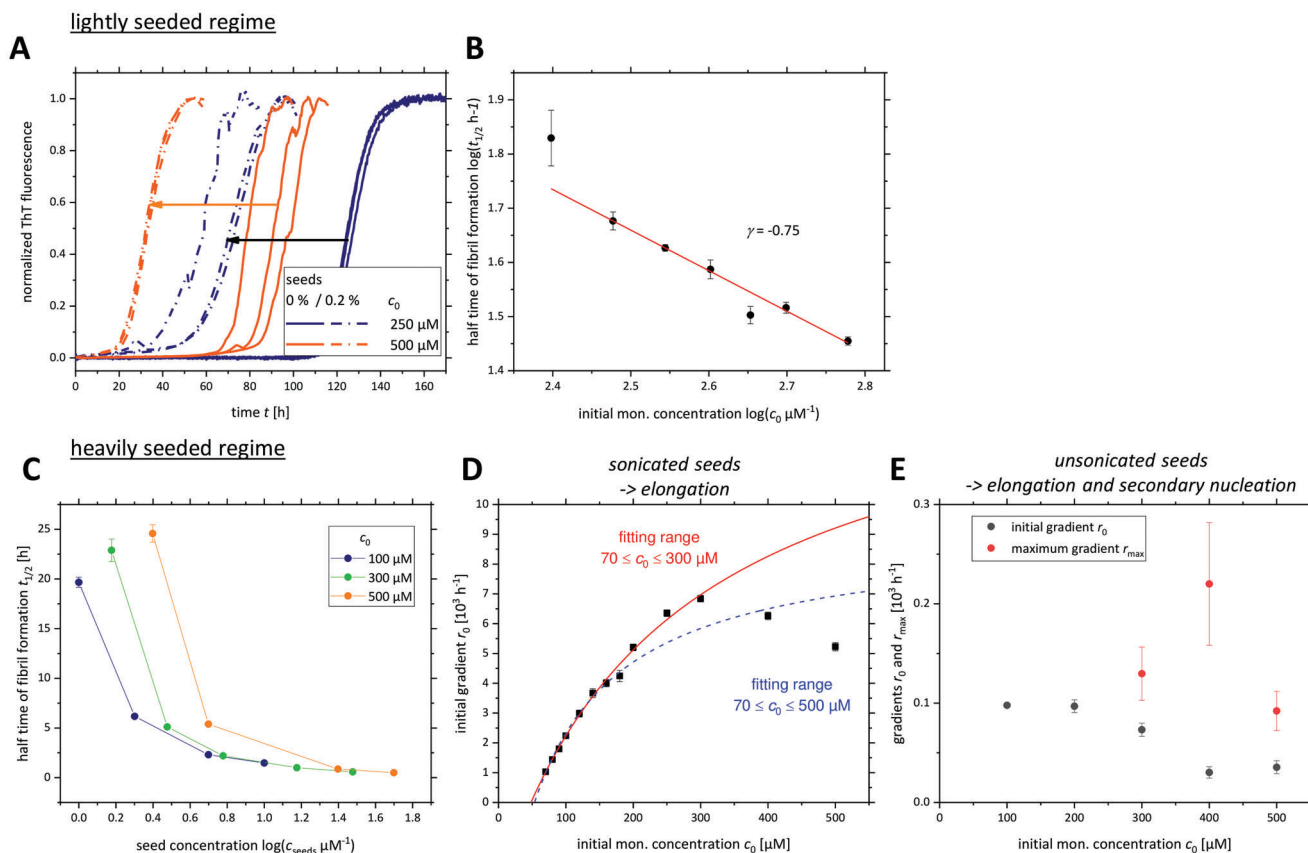
Figure 4. Seeding experiments reveal the importance of secondary processes as well as inhibition effects. A) Comparison of fibril formation de novo (solid lines) with the addition of 0.2 % seeds (given as monomer equivalents of c_0, dotted lines) for $c_0 = 250$ (blue) and 500 µM (orange). Arrows indicate the shift of the kinetic curves toward lower lag times. The data for de novo fibrillation are the same as presented in Figure 2A. B) $\log(t_{1/2})$-$\log(c_0)$-plot of the half times. The scaling factor was found to be $\gamma = -0.75$. Additional curves are shown in Figure S2A, Supporting Information. C) $t_{1/2}$-$\log(c_0)$-plot of PTH$_{84}$ at three different c_0 with different amounts of sonicated seeds added at time zero. Seed concentrations are given as monomer equivalents of c_0. The solid lines connecting the data points are drawn to guide the eye. D) initial gradients r_0 at various c_0 supplemented with 25 µM sonicated seeds. The dashed blue and the solid red lines are fits according to Equation (2) in the c_0 ranges 70–500 µM or 70–300 µM, respectively. E) initial (black) and maximum gradients (red) r_0 and r_{max}, respectively, of various c_0 supplemented with unsonicated seeds. For 100 and 200 µM no further fluorescence increase was found after the initial phase. All data points represent the mean and the standard deviation of three individual replicates.

are effectively bypassed (Figure 4B). With the addition of seeds, elongation and secondary nucleation directly proceed from these templates, whereas the relevance of primary nucleation becomes negligible.

2.3.2. Heavy Seeding Reveals that Elongation as well as Secondary Nucleation are Affected by High Peptide Concentrations

In order to evaluate if saturation of the elongation rate constant k_+ is responsible for the positive curvature of the halftime plot (Figure 2D), we performed additional seeding experiments (Figure 4C–E). In contrast to the presented data at very low c_{seed}, elongation of the existing seeds is the only significant contribution to the increase in fibrillar mass in the high seeding regime. This can be addressed as the linear initial gradient of the ThT signal r_0 at the first points of the time course. The dependence of r_0 from c_0 for a constant seed number concentration P_0 is given by

$$r_0 \sim \left.\frac{dM}{dt}\right|_{t\to 0} = 2\,k_+\,c_0 P_0 \qquad (1)$$

with M the aggregate mass concentration and k_+ the rate constant of elongation.[14] P_0 reflects the number of template fibrils in a seed sample, in contrast to c_{seed} which denotes the seed mass concentration. Since P_0 is a highly error-prone parameter, we do not aim to calculate k_+. To determine the necessary seed mass concentration c_{seed} at which the high seeding regime can be expected we performed seeding experiments at increasing c_{seed} with three different monomer concentrations (with c_{seed} up to 10 % of c_0, in monomer equivalents). Directly plotting the halftime of aggregation versus the logarithm of c_{seed} allows an estimation on the regime (Figure 4C and Figure S2B, Supporting Information). The high seeding regime is expected for a linear dependence with a small negative slope. We identified $c_{seed} = 25$ µM to fulfill these requirements (at $\log(c_{seed}) = 1.4$ in Figure 4C). At lower seed concentrations, the non-linear nature of the plot proves the contribution of secondary processes. Interestingly, at a given c_{seed} in this range, we obtained a concentration dependent t_m, possibly indicating inhibitory effects at high c_0.

In the next step, PTH$_{84}$ at varying monomer concentrations was supplemented at time zero with a constant seed mass

**ADVANCED
SCIENCE NEWS**

www.advancedsciencenews.com

[M] acro-
molecular
Bioscience

www.mbs-journal.de

concentration of $c_{\mathrm{seed}} = 25$ μM (Figure 4D and Figure S2C, Supporting Information). We found a linear dependence of the initial gradient r_0 from c_0 for $c_0 \leq 200$ μM, indicative for monomers as the species required for elongation.[38] The addition of oligomers to fibril ends would result in a polynomial-like dependence.[39] However, with a maximum at 300 μM a further increase of c_0 even results in a decrease of r_0. The data indicate that the rate constant of elongation, k_+, is not proportional to c_0, as predicted by the halftime plot (Figures 2D and 4C), and is written as $\tilde{k}_+$. For the case of a saturation of the elongation process, Equation (1) needs to be extended to

$$r_0 = 2\,\tilde{k}_+ c_0 P_0 = \frac{2\,k_+\,c_0}{1 + \frac{c_0}{K_E}}\,P_0 + \gamma_0 \tag{2}$$

in analogy to the Michaelis–Menten description of enzymatic reactions, with k_+ the true rate constant of elongation, K_E the concentration at which saturation effects occur and γ_0 an offset value introduced due to the high value of c_c below which no fibril formation occurs.[40] In this case diffusion and binding of a monomer to a growth-competent end ("dock") is the rate-determining step at low c_0, whereas the slow structural conversion becomes limiting at high c_0 when basically all free ends are blocked by attached monomers ("lock"). A fit of the data to Equation (2) is shown in Figure 4D (blue dotted line). The fit only succeeds to represent the data at low c_0 but fails at high c_0. However, a systematic decrease of r_0 at high c_0 is obvious from the experimental kinetic curves (Figure S2C, Supporting Information). We further confined the fitting range to the maximum value of r_0 (red solid line in Figure 4D) resulting in a valuable fit within this range. Interestingly, the model of saturated elongation reaches a limitation when applied to our data. We suspect that the elongation step at high c_0 is confined by an inhibition rather than by a true saturation effect.

Note that for this experiment the seeds have been probe-sonicated to break the fibrils into fragments and thus to increase the number of growth competent ends ($2\,P_0$ in Equation (1) and (2), Figure S1C, Supporting Information). The same experiment can be conducted for untreated seeds displaying an essentially lower number of free ends compared to the fibril mass (Figure 4E and Figure S2D, Supporting Information). This allows conclusions on secondary processes. If secondary processes are active, the initial gradient r_0 is not equal to the maximum slope r_{max}. A relation of r_{max} to the time evolution of the fibril number concentration, predominantly reflecting secondary processes in the observed time regime, is given by

$$r_{\mathrm{max}} \sim \frac{dP_t}{dt} \sim k_2 M_t c_0^{n_2} + 2\,k_- P_t \tag{3}$$

where P_t and M_t are the fibril number and fibril mass concentration, respectively, k_2 and n_2 the rate constant and reaction order of secondary nucleation, respectively, according to the two-step bulk description, and k_- the rate constant of fragmentation.[14,41,42] The contribution of primary nucleation is neglected in Equation (3). For the initial gradient we found a monomer dependence similar to the behavior described for probe-sonicated seeds. r_0 decreases for $c_0 > 200$ μM. Simultaneously, r_{max} increases, with a maximum at $c_0 = 400$ μM and a decrease at $c_0 = 500$ μM.

Since r_{max} obviously depends on c_0, we propose that secondary nucleation contributes to PTH_{84} fibril formation, rather than monomer independent fragmentation (Equation (3)). Additionally, the data provide a hint toward a saturation or even an inhibition of secondary nucleation at high c_0, in addition to the discussed effect on elongation.

2.4. Kinetics of PTH_{84} Amyloid Formation Display a Complex Concentration Dependence

In order to gain a deeper understanding of the underlying mechanism of amyloid formation by PTH_{84} we performed individual curve fittings to the increasing part of the ThT monitored fibrillation kinetics depicted in Figure 2A (Equation (6)) as described previously, thus revealing information about the effective rates of primary (λ) and secondary (κ) processes.[25] The fits reproduce the data well, only at $c_0 = 600$ μM (red curve) it is obvious that the applied simple model is not sufficient to describe the full curve (**Figure 5**A). Still, the parameters provide a solid trend. As mentioned before, the introduction of a second component contributing to the overall fibrillation kinetic is necessary to describe the data at c_0 below 200 μM (Equation (17)). Since the percentage of the second kinetic component approaches < 5 % with increasing c_0, and thus giving high errors of the fitting parameters, we only focused on the dominant first component (Figure S1A, , Supporting Information inset). At c_0 below 250 μM, λ exhibits a linear scaling, though the scattering of the data points did not allow a well-defined fit (Figure 5B). The visible trend agrees with a reaction order of $n_{\mathrm{oligo},1} + n_{\mathrm{conv}} \leq 4$ (Equation (9), reaction orders 2 (dotted orange line) and 4 (dashed orange line) are shown as theoretical examples). For higher c_0 the reaction order increases to $n_{\mathrm{oligo},1} + n_{\mathrm{conv}} = 18.5$. These data indicate that the species involved in primary nucleation changes from a low-order oligomer ($n_{\mathrm{oligo},1} + n_{\mathrm{conv}} \leq 4$) to a high-order oligomer ($n_{\mathrm{oligo},1} + n_{\mathrm{conv}} = 18.5$). Note that the reaction order denotes a combination of the respective reaction orders of oligomer formation and oligomer conversion, and thus does not reflect the exact number of monomers within a hypothetical oligomer. Nevertheless, it provides a clear trend. This, highly hypothetical, size of primary nuclei is consistent with a simulation study in which peptides with a low propensity to form β-sheets were found to have higher corresponding primary nuclei sizes of $n_1 > 2$ compared to, for example, $A\beta_{40}$.[43] PTH_{84} is known to exhibit an α-helical propensity at the N-terminus while the C-terminal region remains intrinsically disordered.[22,23]

The importance of the air-water-interface (AWI), and thus the surface tension, is a mostly neglected but underappreciated factor in amyloid growth.[44] The surface tension of a solution of insulin was shown to decrease if oligomers are present, but increased for a fibril-containing sample.[45] In general, conformational and oligomerization effects at the AWI have been reported, for example, β-sheet containing dimer formation and induced polymorphism via alternative assembly pathways.[44,46–48] For example, amphipathic helices display an inherent surface activity.[49] For PTH_{84} residues S17-V31 are reported to adopt such an amphipathic helical structure, which in the context of hormone activity is required for receptor activation.[50] As a consequence, small oligomers of PTH_{84} which are possibly formed and converted
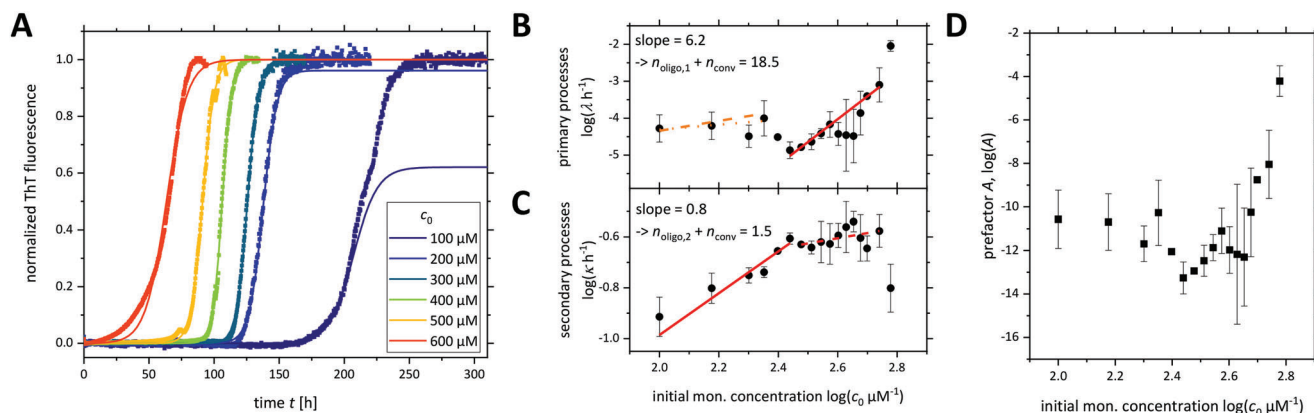
Figure 5. Individual curve fitting reveals insights into primary and secondary processes. The data shown in Figure 2A have been fitted according to Equation (7). A) Representative curves chosen from triplicate measurements (points) at six individual c_0 with the respective fits (solid lines) are shown. For 100 and 200 μM Equation (17) was used, introducing a second kinetic component. The fits and the data in the following panels are only given for the first component. The extracted parameters are B) λ, the sum of primary, C) κ, the sum of secondary processes and D) the kinetic prefactor A (Equation 8). In B–D) the parameters are presented as log(parameter)-log(c_0)-plots. Concentration ranges in panels B) and C) displaying a respective linear scaling are indicated with a solid red line corresponding to a power law fit with $\log(\lambda/\kappa) = \text{slope}_{\lambda/\kappa} \times \log(c_0) + \text{constant}_{\lambda/\kappa}$. All data points represent the mean and the standard deviation of three individual replicates. The orange lines in panel B) represent theoretical curves for $n_{\text{oligo},1} + n_{\text{conv}} = 2$ (dotted) and $n_{\text{oligo},1} + n_{\text{conv}} = 4$ (dashed).

to an elongation competent nucleus at low c_0 by adsorption of the amphipathic helix at the AWI via different pathways could be a considerable origin of the here observed polymorphism (Figure 3A).

For the investigation of κ we only took $c_0 \leq 275$ μM into account considering the high statistical errors of the data points at higher c_0 and the inhibition effects at high c_0 (compare with Figure 4D,E), resulting in the reaction order $n_{\text{oligo},2} + n_{\text{conv}} = 1.5$ (Equation (10), Figure 5C). Equation (16) shows that this corresponds to the more frequently used bulk model with $n_2 = 0.7$, indicating a peptide monomer as the physical nucleus size required for secondary nucleation. Thus, we note that both elongation (Figure 4D) and secondary nucleation (Figures 4E and 5C), the microscopic processes requiring monomeric peptide, are inhibited at high c_0. However, at 300 μM, a concentration at which the half-time scaling factor was found to approach $\gamma = 0$ (Figure 2D), the scaling of κ apparently becomes concentration independent. The definition of κ includes elongation (k_+) as well as secondary nucleation ($k_{\text{oligo},2} k_{\text{conv}}$) (Equation (10)). The apparent saturation of κ might be an effect of the inhibition of one or both processes (see also Figure 4D,E). Interestingly, the high reaction order of λ obviously compensates the effect of k_+ on the c_0 dependence of λ. Nevertheless, the contribution of a high-order oligomer is evident. The high hypothesized order of an involved oligomer raises the question if this indicates a "core–shell" nanocrystal or a micelle- or droplet-like condensed state.[51] Interestingly, for lysozyme, IAPP and α-synuclein it has been shown that nucleation from such states result in very weak dependences on c_0 which is in contrast to our data.[48,52–54]

The significantly different reaction orders of primary and secondary nucleation, in combination with a negative curvature in the halftime plot, gives rise to the hypothesis that primary nucleation starts to compete with secondary processes at high c_0 to be the dominant mechanism of new fibril generation. To the best of our knowledge, this is the first experimental report of this specific case. An inspection of the prefactor A ($A = \lambda^3 \, 3^{-1} \, \kappa^{-3}$, Equa-

tion (8)) illustrates this behavior. From this definition it follows that small values ($A < 0.33$ for $\lambda = \kappa$) or a negative trend indicate the dominance of secondary processes. At low c_0, A is of the order 10^{-11} with a negative dependence on c_0, highlighting the importance of secondary processes on the macroscopic fibrillation curves (Figure 4C). A dramatic increase of A of several orders of magnitude after passing a minimum at 275 μM indicates the competition of two microscopic mechanisms to be the dominant process for the creation of new growth-competent ends, P_0, and thus the relevance of primary nucleation for high c_0.

3. Conclusion

In this work we investigated amyloid fibril formation of PTH_{84}. Employing a simple kinetic analysis approach, we have been able to elucidate an intricate concentration-driven fibrillation network of a functional amyloid (**Figure 6**). We demonstrated a complex concentration dependent behavior including polymorphism, assembly of fibrils into clusters and inhibition effects. We found that at low c_0 (for $c_0 > c_c$) fibrils nucleate from small oligomeric peptide species. The variation of the fibril diameters agrees with the occurrence of, at least, two distinguishable kinetic components contributing to the overall fibrillation behavior. At low concentrations ($c_0 < 300$ μM), secondary nucleation is the dominant process for the creation of new fibrils. Upon increasing c_0, the monomer consuming processes elongation and secondary nucleation become inhibited. In addition, the physical size of the primary nucleus dramatically increases, indicating a different underlying nucleation mechanism. We conclude that the nucleus originates from large on-pathway oligomers which are in equilibrium with monomers above a certain threshold concentration, the "critical oligomer concentration" (coc), reducing the effective monomer concentration. Thus, monomer availability becomes rate limiting for self-propagation (secondary nucleation) and the increase in fibrillar mass (elongation).
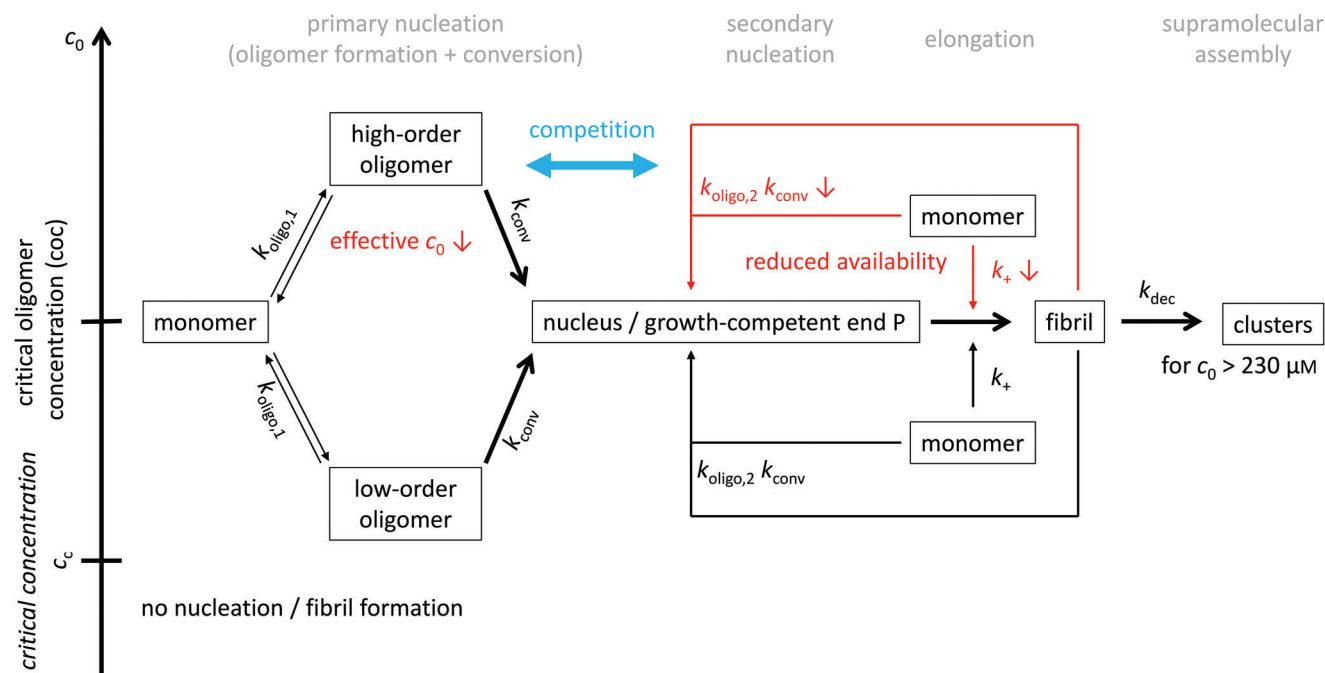
Figure 6. Scheme of the concentration dependence of PTH_{84} amyloid fibril growth. Below the critical concentration c_c, PTH_{84} is monomeric and no fibril formation occurs. Above the c_c low-order oligomers or, when exceeding a threshold concentration, coc, high-order oligomers of PTH_{84} contribute to the formation of primary fibril nuclei. Both oligomer species are on-pathway within the fibrillation network. The equilibrium decreases the concentration of available monomers (apparent c_0), negatively affecting elongation and secondary nucleation as the processes requiring monomers (indicated by red arrows). Moreover, exceeding a solubility barrier fibrils self-assemble into supramolecular clusters that eventually precipitate with a rate constant independent from c_0. However, below the coc secondary nucleation is the dominant process producing new growth-competent ends P, but competes with primary nucleation above the coc.

In addition, fibril precipitation occurs above a threshold concentration of $c_0 = 230\ \mu M$, indicating a maximum soluble fibril fraction of $163\ \mu M$ (given in monomer equivalents converted into fibrils) in equilibrium with free monomers. The occurrence of two distinct linear regimes of the maximum ThT fluorescence intensities results from the different origins of primary nuclei at low or high c_0. We suspect that the nature of the nucleus determines the exact fibril morphology and thus the ThT binding behavior. This is supported by the concentration dependent polymorphism of PTH_{84} fibrils as well as by the observed photophysical changes of fibril bound ThT occurring only at high c_0.

Furthermore, we revealed PTH_{84} to be an amyloid forming system exhibiting primary nucleation with a high reaction order able to kinetically compete with secondary nucleation to be the dominant process for the generation of new fibrils. This is, according to our knowledge, the first experimental report of such a scenario. A more detailed investigation of the hypothesized PTH_{84} concentration dependent monomer-oligomer equilibrium will be part of our future work.

4. Experimental Section

Chemicals: All chemicals were purchased from Carl Roth GmbH or Sigma Aldrich and used without further purification.

Recombinant Production and Purification of PTH_{84}: PTH_{84} was produced recombinantly in *E. coli* BL21 (DE3) c+ RIL cells and purified from the cell lysate as described previously with small changes.[24,55] The established purification procedure consisted of immobilized metal ion affin-

ity chromatography (Ni^{2+}-IMAC), hydrophobic interaction chromatography (HIC), and size exclusion chromatography (SEC). In contrast to the published protocol a cation exchange chromatography step (CIEX using a sulphopropyl residue) was conducted, followed by subsequent dialysis (3.5 kDa molecular weight cut-off) in 50 mM Na_2HPO_4, pH7.4. The peptide was stored as a 1 mM stock solution in the same buffer at −80 °C.

ThT Fluorescence Monitored Kinetic Fibrillation Assay: The PTH_{84} stock solution was carefully thawed on ice. After subsequent centrifugation at 12 800× g for 1 h at 4 °C to remove possible pre-formed aggregates, the supernatant was used to adjust the desired PTH_{84} monomer concentrations. NaCl was added to a final concentration of 150 mM from a stock (50 mM Na_2HPO_4, 3 M NaCl, pH7.4). The small, extended β-sheet specific dye Thioflavin T (ThT) was used to monitor the increasing fibril mass.[56] The concentration of ThT was adjusted to 45 μM in all samples from a 1 mM stock.

The measurements were performed in triplicates from the same samples on the same black non-binding 96-well plates with transparent bottom (Greiner Bio-One, Art. Nr. 655 906). The plates were sealed to prevent evaporation. ThT fluorescence indicating fibril growth was monitored at 37 °C in a FluoStar Omega plate reader using bottom optics (BMG Labtech). For excitation (448 nm) and emission (482 nm) optical filters were used with 10 nm bandwidth. Depending on the experimental requirements, two different incubation protocols have been designed:

Protocol I: 30 s double-orbital shaking at 300 rpm, 270 s quiescent incubation
Protocol II: 5 s double-orbital shaking at 300 rpm, 295 s quiescent incubation

For monomer dependent de novo nucleation and low seeding experiments, protocol I was applied with fluorescence detection in a cycle of 20 min. Protocol II (5 min cycle) was used for heavily seeded experiments.

Equilibrium Free Monomer and ThT Concentrations: Fibrillation samples in the thermodynamic equilibrium were centrifuged at 16 100× g for 1 h at room temperature. The concentration of free peptide monomer in solution was determined at 280 nm ($\epsilon_{280} = 5500$ м$^{-1}$ cm^{-1}) and of free ThT at 412 nm ($\epsilon_{412} = 36\,000$ м$^{-1}$ cm^{-1}) by UV–vis spectroscopy.[57,58] Since ThT contributes to the UV absorption at 280 nm, the peptide absorption was corrected using Equation (4)

$$OD_{280,peptide} = OD_{280} - OD_{412}\, \frac{OD_{280,ref}}{OD_{412,ref}} \quad (4)$$

where $OD_{280,ref}$ and $OD_{412,ref}$ are the corresponding absorption values of ThT in a reference sample without peptide. The molar concentrations were calculated with the law of Lambert–Beer. The baseline correction was conducted with pure buffer.

Seed Preparation: Seeds were prepared from a 500 µм fibrillation sample without ThT which reached the stationary phase. If not mentioned otherwise, fibrils were disrupted by probe-sonication (1 s pulse, 1 s pause, 12 × 10 % amplitude). Seeded assays were started within maximally 30 min after seed preparation.

Optical Density and Scattering: After completion of the kinetic assay, UV–vis spectra had subsequently been acquired for all replicates without removing the seal foil (FluoStar Omega, BMG Labtech; range 350–700 nm, data pitch 5 nm). For the characterization of the ThT absorbance the ratio of the optical density OD at 420 and 430 nm ($OD_{420}\,OD_{430}^{-1}$) was calculated. This work defined the observed turbidity of the samples to be the scattering intensity, that is, as the increase of OD_{600} of a respective sample compared to the control that only contained ThT:

$$scattering = OD_{600,\,sample} - OD_{600,\,control} \quad (5)$$

Kinetic Analyses: The fluorescence decay after passing a maximum value was fitted with a single exponential function

$$F = F_0 + Be^{-k_{dec}t} \quad (6)$$

with k_{dec} the exponential decay rate.

For the investigation of the mechanism of PTH$_{84}$ fibril formation a simple kinetic approach was employed as described previously.[17,25,59] For a basic description of the sigmoidal curve shape the introduction of the parameters λ and κ reflecting the sum of primary and secondary events, respectively, results in the function

$$F_t = 1 - \frac{1}{1 + A(e^{\kappa t} - 1)} \quad (7)$$

with F the normalized ThT fluorescence and the parameters

$$A = \frac{\lambda^3}{3\,\kappa^3} \quad (8)$$

$$\lambda = (2\,k_+\,k_{oligo,1}\,k_{conv}\,c_0^{n_{oligo,1}+n_{conv}})^{1/3} \quad (9)$$

$$\kappa = (2k_+\,k_{oligo,2}\,k_{conv}\,c_0^{n_{oligo,2}+n_{conv}+1})^{1/3} \quad (10)$$

with $k_{oligo,1/2}$ the rate constant of the formation of oligomers involved in primary or secondary nucleation, respectively, k_{conv} the rate constant of conversion, k_+ the rate constant of elongation via monomer addition, c_0 the initial peptide monomer concentration, $n_{oligo,1/2}$ the reaction order of the formation of oligomers involved in primary or secondary nucleation, respectively, and n_{conv} the reaction order of oligomer conversion. The reaction orders can be extracted from the corresponding $\log(\lambda/\kappa)$-$\log(c_0)$-plots with the scaling factors.

$$\gamma_\lambda = \frac{n_{oligo,1} + n_{conv}}{3} \quad (11)$$

$$\gamma_\kappa = \frac{n_{oligo,2} + n_{conv} + 1}{3} \quad (12)$$

This approach explicitly takes nucleation via oligomeric species into account which is reflected by the cubic influence of λ and κ on the prefactor A and thus on the time scale. In this case nucleation is treated as a three-step process consisting of oligomer formation ($k_{oligo,1/2}$), conversion of the oligomers into growth-competent species (k_{conv}) and elongation (k_+), with the respective reaction orders $n_{oligo,1/2}$ and n_{conv}.

A connection to the more frequently used two-step description (nucleation coupled with elongation) with the bulk rate constants k_1 and k_2 and the corresponding bulk reaction orders n_1 and n_2 of primary and secondary nucleation, respectively, is given by:

$$k_1 = \frac{2}{3}\left(\frac{k_{oligo,1}^3\,k_{conv}^2}{2\,k_+\,k_{oligo,2}}\right)^{1/3} \quad (13)$$

$$k_2 = \left(\frac{k_2^{oligo,2}\,k_2^{conv}}{2\,k_+}\right)^{1/3} \quad (14)$$

$$n_1 = n_{oligo,1} - n_{oligo,2} + n_2 \quad (15)$$

$$n_2 = \frac{2\,n_{oligo,2} + 2\,n_{conv} - 1}{3} \quad (16)$$

For low concentrations, a second kinetic component was added to Equation (7), which leads to

$$F = F_{tot} - \frac{F_1}{1 + A_1(e^{\kappa_1 t} - 1)} + \frac{(F_{tot} - F_1)}{1 + A_2(e^{\kappa_2 t} - 1)} \quad (17)$$

with F_{tot} the total fluorescence signal, F_1 the fluorescence of component 1, $A_{1/2}$ and $\kappa_{1/2}$ the kinetic prefactor and the sum of secondary events for the first or the second component, respectively. The major kinetic component is indexed as "1."

Negative-Staining Electron Microscopy: The fibrillation samples were diluted 20-fold in buffer (50 mм Na$_2$HPO$_4$, 150 mм NaCl, pH 7.4) and subsequently 5 µL were transferred to a 3 mm carbon/Formvar-coated copper grid. After 3 min incubation, the grids were blotted, washed with ddH$_2$O and blotted again. For negative staining, grids were incubated with 1 % uranyl acetate. After blotting, the grids were allowed to dry for 24 h on filter paper. Sample imaging was conducted on a Zeiss EM900 electron microscope with 80 kV acceleration voltage. The analyses of the fibril diameters as well as the cross-section gray-scale profiles were performed using ImageJ/Fiji software. The diameters were calculated based on the measurement of $n = 100$ ($c_0 = 100$ µм), $n = 75$ ($c_0 = 300$ µм), or $n = 30$ ($c_0 = 500$ µм) fibrils.

Supporting Information

Supporting Information is available from the Wiley Online Library or from the author.

Acknowledgements

Conflict of Interest

The authors declare no conflict of interest.

Data Availability Statement

The data that support the findings of this study are available from the corresponding author upon reasonable request.

[1] F. Chiti, C. M. Dobson, *Annu. Rev. Biochem.* **2006**, *75*, 333.
[2] D. Otzen, R. Riek, *Cold Spring Harb. Perspect. Biol.* **2019**, *11*, a033860.
[3] M. R. Chapman, L. S. Robinson, J. S. Pinkner, R. Roth, J. Heuser, M. Hammar, S. Normark, S. J. Hultgren, *Science* **2002**, *295*, 851.
[4] D. M. Fowler, A. V. Koulov, C. Alory-Jost, M. S. Marks, W. E. Balch, J. W. Kelly, *PLoS Biol.* **2006**, *4*, e6.
[5] R. Hervas, M. J. Rau, Y. Park, W. Zhang, A. G. Murzin, J. A. J. Fitzpatrick, S. H. W. Scheres, K. Si, *Science* **2020**, *367*, 1230.
[6] S. K. Maji, M. H. Perrin, M. R. Sawaya, S. Jessberger, K. Vadodaria, R. A. Rissman, P. S. Singru, K. P. R. Nilsson, R. Simon, D. Schubert, D. Eisenberg, J. Rivier, P. Sawchenko, W. Vale, R. Riek, *Science* **2009**, *325*, 328.
[7] A. Anoop, S. Ranganathan, B. D. Dhaked, N. N. Jha, S. Pratihar, S. Ghosh, S. Sahay, S. Kumar, S. Das, M. Kombrabail, K. Agarwal, R. S. Jacob, P. Singru, P. Bhaumik, R. Padinhateeri, A. Kumar, S. K. Maji, *J. Biol. Chem.* **2014**, *289*, 16884.
[8] R. S. Jacob, S. Das, S. Ghosh, A. Anoop, N. N. Jha, T. Khan, P. Singru, A. Kumar, S. K. Maji, *Sci. Rep.* **2016**, *6*, 23370.
[9] S. K. Maji, D. Schubert, C. Rivier, S. Lee, J. E. Rivier, R. Riek, *PLoS Biol.* **2008**, *6*, e17.
[10] N. Nespovitaya, J. Gath, K. Barylyuk, C. Seuring, B. H. Meier, R. Riek, *J. Am. Chem. Soc.* **2016**, *138*, 846.
[11] K. C. Evans, E. P. Berger, C. G. Cho, K. H. Weisgraber, P. T. Lansbury, *Proc. Natl. Acad. Sci. U.S.A.* **1995**, *92*, 763.
[12] L. Nielsen, R. Khurana, A. Coats, S. Frokjaer, J. Brange, S. Vyas, V. N. Uversky, A. L. Fink, *Biochemistry* **2001**, *40*, 6036.
[13] T. C. T. Michaels, A. Šarić, J. Habchi, S. Chia, G. Meisl, M. Vendruscolo, C. M. Dobson, T. P. J. Knowles, *Annu. Rev. Phys. Chem.* **2018**, *69*, 273.
[14] S. I. A. Cohen, M. Vendruscolo, M. E. Welland, C. M. Dobson, E. M. Terentjev, T. P. J. Knowles, *J. Chem. Phys.* **2011**, *135*, 065105.
[15] F. Oosawa, M. Kasai, *J. Mol. Biol.* **1962**, *4*, 10.
[16] G. Meisl, L. Rajah, S. A. I. Cohen, M. Pfammatter, A. Šarić, E. Hellstrand, A. K. Buell, A. Aguzzi, S. Linse, M. Vendruscolo, C. M. Dobson, T. P. J. Knowles, *Chem. Sci.* **2017**, *8*, 7087.
[17] T. C. T. Michaels, A. Šarić, S. Curk, K. Bernfur, P. Arosio, G. Meisl, A. J. Dear, S. I. A. Cohen, C. M. Dobson, M. Vendruscolo, S. Linse, T. P. J. Knowles, *Nat. Chem.* **2020**, *12*, 445.
[18] Z. Agus, L. Gardner, L. Beck, M. Goldberg, *Am. J. Physiol.* **1973**, *224*, 1143.
[19] R. R. MacGregor, D. V. Cohn, *Clin. Orthop. Relat. Res.* **1978**, *137*, 244.
[20] J. F. Habener, J. T. Potts, *N. Engl. J. Med.* **1978**, *299*, 580.
[21] K. M. Wiren, J. T. Potts, H. M. Kronenberg, *J. Biol. Chem.* **1988**, *263*, 19771.
[22] M. Gopalswamy, A. Kumar, J. Adler, M. Baumann, M. Henze, S. T. Kumar, M. Fändrich, H. A. Scheidt, D. Huster, J. Balbach, *Biochim. Biophys. Acta* **2015**, *1854*, 249.
[23] U. C. Marx, S. Austermann, P. Bayer, K. Adermann, A. Ejchart, H. Sticht, S. Walter, F. X. Schmid, R. Jaenicke, W. G. Forssmann, P. Rösch, *J. Biol. Chem.* **1995**, *270*, 15194.
[24] Z. Evgrafova, B. Voigt, M. Baumann, M. Stephani, W. H. Binder, J. Balbach, *ChemPhysChem* **2019**, *20*, 236.
[25] L. M. Lauth, B. Voigt, T. Bhatia, L. Machner, J. Balbach, M. Ott, *FEBS Lett.* **2022**, *596*, 2928.
[26] J. S. Wall, T. Richey, A. Stuckey, R. Donnell, S. Macy, E. B. Martin, A. Williams, K. Higuchi, S. J. Kennel, *Proc. Natl. Acad. Sci. U.S.A.* **2011**, *108*, E586.
[27] I. Kedar, M. Ravid, E. Sohar, *Isr. J. Med. Sci.* **1976**, *12*, 1137.
[28] Z. Evgrafova, S. Rothemund, B. Voigt, G. Hause, J. Balbach, W. H. Binder, *Macromol. Rapid. Commun.* **2020**, *41*, 1900378.
[29] Z. Evgrafova, B. Voigt, A. H. Roos, G. Hause, D. Hinderberger, J. Balbach, W. H. Binder, *Phys. Chem. Chem. Phys.* **2019**, *21*, 20999.
[30] S. Deike, S. Rothemund, B. Voigt, S. Samantray, B. Strodel, W. H. Binder, *Bioorg. Chem.* **2020**, *101*, 104012.
[31] A. Paschold, B. Voigt, G. Hause, T. Kohlmann, S. Rothemund, W. H. Binder, *Biomedicines* **2022**, *10*, 1512.
[32] G. Meisl, X. Yang, E. Hellstrand, B. Frohm, J. B. Kirkegaard, S. I. A. Cohen, C. M. Dobson, S. Linse, T. P. J. Knowles, *Proc. Natl. Acad. Sci. U.S.A.* **2014**, *111*, 9384.
[33] R. Khurana, C. Coleman, C. Ionescu-Zanetti, S. A. Carter, V. Krishna, R. K. Grover, R. Roy, S. Singh, *J. Struct. Biol.* **2005**, *151*, 229.
[34] D. J. Lindberg, A. Wenger, E. Sundin, E. Wesén, F. Westerlund, E. K. Esbjörner, *Biochemistry* **2017**, *56*, 2170.
[35] G. Sancataldo, V. Anselmo, V. Vetri, *Microsc. Res. Tech.* **2020**, *83*, 811.
[36] J. D. Harper, P. T. Lansbury, *Annu. Rev. Biochem.* **1997**, *66*, 385.
[37] D. C. Rodriguez Camargo, E. Sileikis, S. Chia, E. Axell, K. Bernfur, R. L. Cataldi, S. I. A. Cohen, G. Meisl, J. Habchi, T. P. J. Knowles, M. Vendruscolo, S. Linse, *ACS Chem. Neurosci.* **2021**, *12*, 4406.
[38] A. K. Buell, *Biochem. J.* **2019**, *476*, 2677.
[39] T. K. Karamanos, M. P. Jackson, A. N. Calabrese, S. C. Goodchild, E. E. Cawood, G. S. Thompson, A. P. Kalverda, E. W. Hewitt, S. E. Radford, *Elife* **2019**, *8*, e46574.
[40] N. Lorenzen, S. I. A. Cohen, S. B. Nielsen, T. W. Herling, G. Christiansen, C. M. Dobson, T. P. J. Knowles, D. Otzen, *Biophys. J.* **2012**, *102*, 2167.
[41] S. I. A. Cohen, M. Vendruscolo, C. M. Dobson, T. P. J. Knowles, *J. Chem. Phys.* **2011**, *135*, 065106.
[42] S. Linse, *Curr. Opin. Struct. Biol.* **2021**, *70*, 87.
[43] A. Šarić, T. C. T. Michaels, A. Zaccone, T. P. J. Knowles, D. Frenkel, *J. Chem. Phys.* **2016**, *145*, 211926.
[44] L. Jean, C. F. Lee, C. Lee, M. Shaw, D. J. Vaux, *FASEB J.* **2010**, *24*, 309.
[45] E. Kachooei, A. A. Moosavi-Movahedi, F. Khodagholi, H. Ramshini, F. Shaerzadeh, N. Sheibani, *PLoS One* **2012**, *7*, e41344.
[46] E. Y. Chi, S. L. Frey, A. Winans, K. L. H. Lam, K. Kjaer, J. Majewski, K. Y. C. Lee, *Biophys. J.* **2010**, *98*, 2299.
[47] F. Grigolato, P. Arosio, *Biophys. Chem.* **2021**, *270*, 106533.
[48] Q. Han, F. Tao, Y. Xu, H. Su, F. Yang, V. Körstgens, P. Müller-Buschbaum, P. Yang, *Angew. Chem., Int. Ed.* **2020**, *59*, 20192.
[49] L. Wang, D. Atkinson, D. M. Small, *J. Biol. Chem.* **2003**, *278*, 37480.
[50] T. Dean, A. Khatri, Z. Potetinova, G. E. Willick, T. J. Gardella, *J. Biol. Chem.* **2006**, *281*, 32485.
[51] F. Tao, Q. Han, K. Liu, P. Yang, *Angew. Chem., Int. Ed.* **2017**, *56*, 13440.
[52] J. R. Brender, J. Krishnamoorthy, M. F. Sciacca, S. Vivekanandan, L. D'urso, J. Chen, C. La Rosa, A. Ramamoorthy, *J. Phys. Chem. B* **2015**, *119*, 2886.
[53] S. T. Dada, M. C. Hardenberg, L. K. Mrugalla, M. O. McKeon, E. Klimont, T. C. T. Michaels, M. Vendruscolo, *(Preprint) bioRxiv*, https://doi.org/10.1101/2021.09.26.461836, submitted: 09, **2021**.

[54] S. B. Padrick, A. D. Miranker, *Biochemistry* **2002**, *41*, 4694.

[55] E. Bosse-Doenecke, U. Weininger, M. Gopalswamy, J. Balbach, S. M. Knudsen, R. Rudolph, *Protein Expr. Purif.* **2008**, *58*, 114.

[56] H. Levine, *Protein Sci.* **1993**, *2*, 404.

[57] G. V. De Ferrari, W. D. Mallender, N. C. Inestrosa, T. L. Rosenberry, *J. Biol. Chem.* **2001**, *276*, 23282.

[58] E. Gasteiger, C. Hoogland, A. Gattiker, S. Duvaud, M. R. Wilkins, R. D. Appel, A. Bairoch, in *The Proteomics Protocols Handbook*, Vol. *1* (Ed: J. M. Walker), Humana Press, Totowa (NJ), USA **2005**, p. 52.

[59] A. J. Dear, T. C. T. Michaels, G. Meisl, D. Klenerman, S. Wu, S. Perrett, S. Linse, C. M. Dobson, T. P. J. Knowles, *Proc. Natl. Acad. Sci. U.S.A.* **2020**, *117*, 12087.